communications materials

Article

https://doi.org/10.1038/s43246-024-00552-x

Perturbation-tuned triple spiral metamagnetism and tricritical point in kagome metal $ErMn_6Sn_6$

Satya Shanmukharao Samatham [1,2], Jacob Casey[2], Adrienn Maria Szucs [3], Venkateswara Yenugonda [2], Christopher Burgio[2], Theo Siegrist[3,4] & Arjun K. Pathak [2,5] ✉

Kagome materials are of topical interest for their diverse quantum properties linked with correlated magnetism and topology. Here, we report anomalous hydrostatic pressure (p) effect on $ErMn_6Sn_6$ through isobaric and isothermal-isobaric magnetization measurements. Magnetic field (H) suppresses antiferromagnetic T_N while simultaneously enhancing the ferrimagnetic T_C by exhibiting dual metamagnetic transitions, arising from the triple-spiral-nature of Er and Mn spins. Counter-intuitively, pressure enhances both T_C and T_N with a growth rate of 74.4 K GPa^{-1} and 14.4 K GPa^{-1} respectively. Pressure unifies the dual metamagnetic transitions as illustrated through p-H phase diagrams at 140 and 200 K. Temperature-field-pressure (T-H, T-p) phase diagrams illustrate distinct field- and pressure-induced critical points at (T_{cr} = 246 K, H_{cr} = 23.3 kOe) and (T_{cr} = 435.8 K, p_{cr} = 4.74 GPa) respectively. An unusual increase of magnetic entropy by pressure around T_{cr} and a putative pressure-induced tricritical point pave a unique way of tuning the magnetic properties of kagome magnets through simultaneous application of H and p.

Topological insulators (TIs) are a new state of matter with unusual electronic configurations. In terms of energy bands, the bulk of these materials behaves like an ordinary insulator (valence and conduction electron bands are separated by a full energy gap), while their edge (surface) acts like a perfect and robust conductor (valence and conduction bands overlapping) topologically protected by time-reversal symmetry. As such, materials showing topological quantum state (also called topological quantum materials, TQMs), display unique and intriguing physical properties which make them promising candidates as main components for technological applications like quantum computers, magnetic storage media, magnetic field sensors, electronic devices, and spintronics[1–8].

Since their discovery, the research on topological materials has attracted great interest in the scientific community, with researchers continuously searching for new topological materials during the past two decades. Among the most investigated systems are the materials crystallizing with a kagome lattice. These materials have shown to be the most prominent for hosting correlated topological states due to the typical kagome geometry where the atoms are arranged into layered sets of overlapping corner-sharing triangles causing destructive quantum interference and "frustration" in the kinetic motion of electrons. As such, kagome lattice systems can support a number of novel quantum phenomena such as the quantum anomalous Hall effect[9], Weyl semimetal[10] Dirac fermions[11,12], Chern quantum phases[13,14], and spin liquid phases[15]. Among the kagome lattice materials hosting topological band structures are, for instance: the binary magnetic compounds TX, T_3X, and T_3X_2 (for T = 3d transition metals and X = Ge, Sn)[16], the ternary $Co_3Sn_2S_2$[17], and $TbMn_6Sn_6$[18]. Interesting is to note that all these materials contain magnetic atoms as a kagome lattice motif, which has an important role in the interplay between magnetic frustration, electronic correlation and topology. Its presence in the crystal structure can, in fact, give rise to further interesting phenomena such as spin-orbit coupling (SOC) and out-of-plane ferromagnetic order. Among the kagome lattice systems containing magnetic atoms is another member of the series RMn_6Sn_6 (R = rare earth)[19–21], still unexplored from the point of view of topological states. The RMn_6Sn_6 compounds for R = Sc, Y, Gd-Tm, and Lu crystallize in the hexagonal $MgFe_6Ge_6$-type (or $HfFe_6Ge_6$-type) [space group *P6/mmm* (No. 191), Pearson's symbol *hP13*][22], where R atoms occupy the *1a* Wyckoff site, Mn atoms fill the *6i* position, and Sn atoms occupy the three symmetry inequivalent *2c*, *2d*, and *2e* sites. The kagome lattice in these compounds is composed of triangular layers of "Mn_3" alternating with layers of "RSn_2" and "Sn_4" along the c-axis. The compounds

[1]Department of Physics, Chaitanya Bharathi Institute of Technology, Gandipet, Hyderabad 500 075, India. [2]Department of Physics, SUNY Buffalo State University, Buffalo, NY 14222, USA. [3]National High Magnetic Field Laboratory, Florida State University, Tallahassee, FL 32310, USA. [4]Department of Chemical and Biomedical Engineering, FAMU-FSU College of Engineering, Tallahassee, FL 32310, USA. [5]Present address: GE Aerospace Research, One Research Circle, Niskayuna, NY 12309, USA. ✉e-mail: pathakak@buffalostate.edu

formed with non-magnetic R (R = Sc, Y, Lu) undergo an AFM ordering of the Mn sublattice at a Neel temperature, T_N, of 333, 353, and 384 K, for YMn_6Sn_6, $LuMn_6Sn_6$, and $ScMn_6Sn_6$, respectively. It may be outlined that the ordering temperature here increases while decreasing the atomic size of the rare earth atom: an example of the resulting effect of the parameter chemical pressure on the physical properties of these compounds. The compounds formed with the magnetic R (R = Gd, Tb, Dy, Ho) show overall a ferrimagnetic (FIM) behavior, given by the simultaneous coupling of the ferromagnetic (FM) ordering of the Mn sublattice with the AFM ordering of the R sublattice. The observed Curie temperatures, T_C, are 435, 423, 393, and 376 K for $GdMn_6Sn_6$, $TbMn_6Sn_6$, $DyMn_6Sn_6$, and $HoMn_6Sn_6$, respectively; in this case, the ordering temperature with the decrease of the atomic size of R atom[23]. Finally, the compounds formed by R = Er and Tm show two separated magnetic transitions: a first AFM ordering occurring at T_N = 352 K and T_N = 347 K for $ErMn_6Sn_6$ and $TmMn_6Sn_6$, respectively, due to ordering of the only Mn sublattice, and an FIM ordering occurring at T_C of 75 K and 58 K for $ErMn_6Sn_6$ and $TmMn_6Sn_6$, respectively, due to the ordering of the R sublattice[24–28]. The transport properties have been measured for several RMn_6Sn_6 compounds[20,29,30]; however, a large topological Hall effect has been observed in YMn_6Sn_6 and $ErMn_6Sn_6$ only[20,31]. Despite all findings about the multiple magnetic orderings and interesting properties of these kagome lattice compounds, much more work still remains to be carried out in order to search for giant and anomalous Hall effects, as well as other topological-related phenomena. In this context, it is interesting to see how the structure, physical, and magnetic properties of RMn_6Sn_6 compounds are affected through physically manipulating by applying hydrostatic pressure. While several works are reported in literature concerning the investigation of RMn_6Sn_6 compounds obtained by atomic substitution of R, Mn, and/or Sn, with other R and T metals and/or another p-block element[31], up to date (at best of our knowledge) there has never been any work concerning the simultaneous effect of hydrostatic pressure and magnetic field on the lattice geometry, physical properties and electronic correlations on any of these compounds.

Polycrystalline $ErMn_6Sn_6$ shows consecutive antiferromagnetic (below 362 K) and ferrimagnetic (below 67 K) transitions along with field-conversion of AFM state to FIM via metamagnetic transitions[32]. Dhakal et al. reported anisotropic and metamagnetic behavior along with topological and anomalous Hall effect in the ferrimagnetic region[31]. However, a comprehensive investigation of the magnetic properties of $ErMn_6Sn_6$ under the influence of external perturbations such as magnetic field and pressure is lacking. In this paper, the effect of magnetic field and pressure (separately and simultaneously) on the magnetic properties of different temperature regions of $ErMn_6Sn_6$ has been investigated. The origin of dual metamagnetic transitions and their evolution with H and p are outlined.

Results

To verify the structural integrity of $ErMn_6Sn_6$ at different temperatures, the sample was ground in an agate mortar, and X-ray powder patterns were acquired using an Anton Paar XRDynamic 500 powder diffractometer equipped with the CHC Plus+ Cryo & Humidity Chamber, configured with liquid nitrogen cooling and under vacuum conditions. Powder pattern measurements were taken at 150, 298, and 380 K with Cu K_α radiation, 0.01° step^{-1} from 5 to 90° 2θ at 100 s/step. The peak fitting and unit cell refinement were conducted using POWDERPLOT by Kenny Stahl (Version 07/07/2016). Data visualizations were generated using the visual data tool, DataGraph (version 5.3). The analysis reveals no structural transformation/distortion of $ErMn_6Sn_6$ as the hexagonal crystal structure of the material remained unchanged over the temperature range studied, as shown in Fig. 1 and refer to Supplementary Note I for more on crystal structure parameters. In addition, both scanning electron microscopy and energy-dispersive spectroscopy findings confirm the material is chemically homogeneous, stoichiometric 1:6:6 phase with no detectable impurities (refer to Supplementary Note II).

The temperature-dependent magnetization of $ErMn_6Sn_6$, measured in H = 0.1 kOe from 2 to 395 K, is shown in Fig. 2a with magnetization M plotted on logarithmic scale measured along $H \parallel ab$-plane. It can be seen

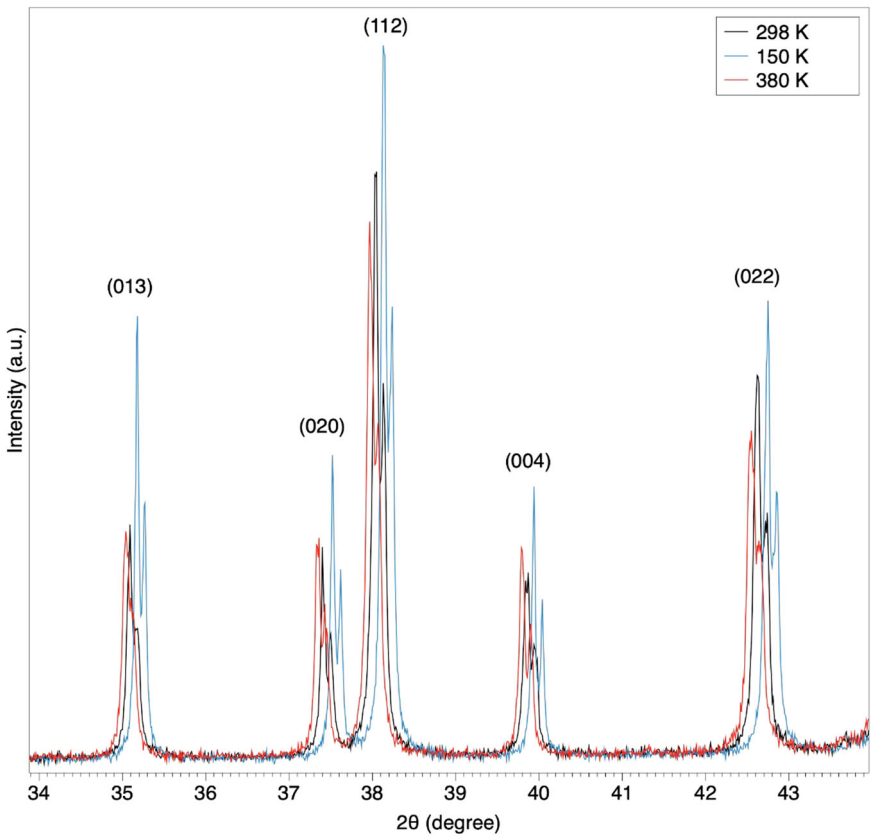

Fig. 1 | The temperature dependent X-ray diffraction patterns of $ErMn_6Sn_6$. Section of the Powder XRD patterns of $ErMn_6Sn_6$ collected at different temperatures 150, 298 and 380 K. The identical patterns indicate no structural change. However, a shift in peaks with temperature is apparent.

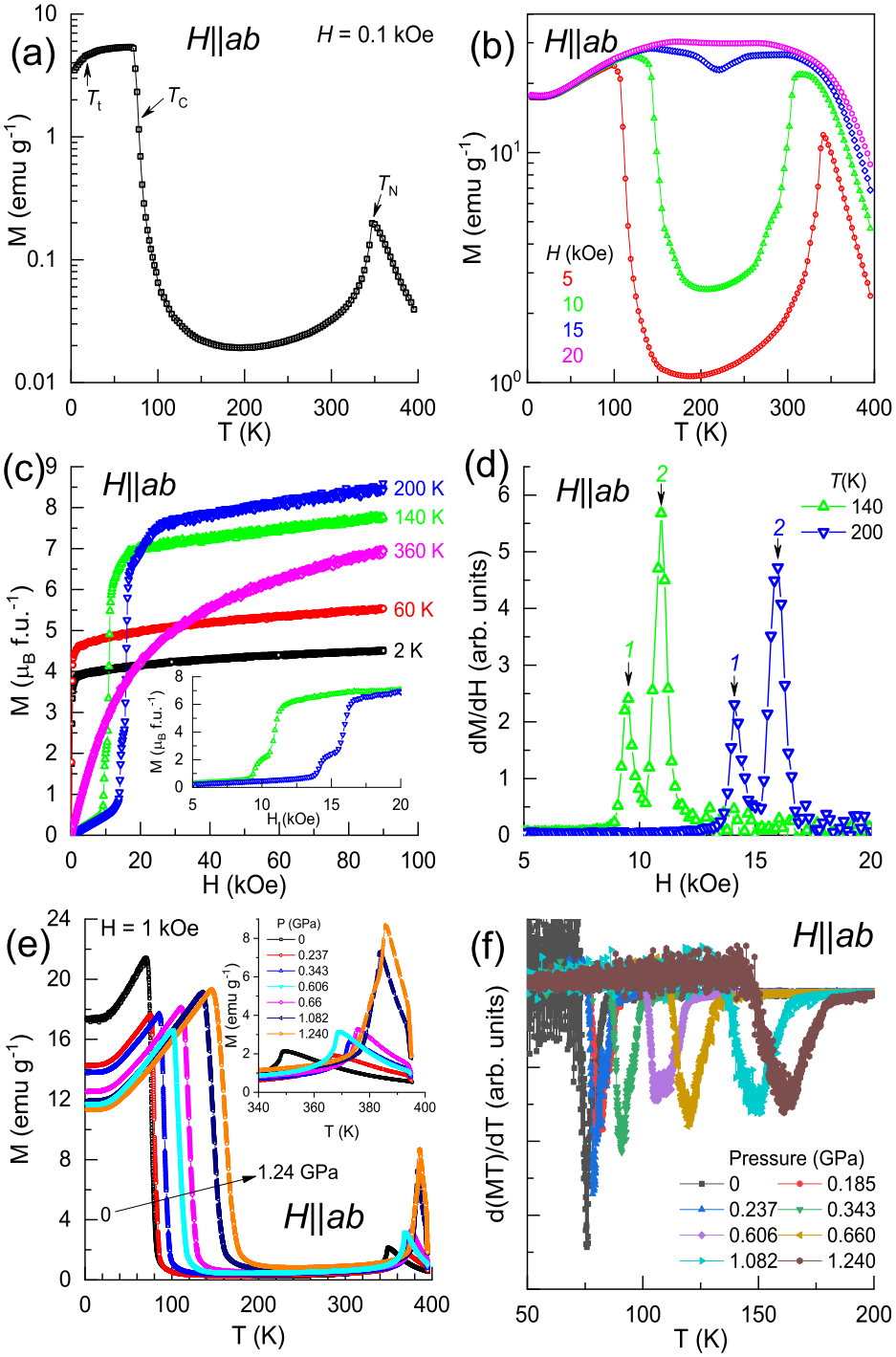

Fig. 2 | Magnetization of $ErMn_6Sn_6$ kagome metal at different temperatures and pressures when the magnetic field is applied parallel to *ab*-plane. The temperature-dependent magnetization of $ErMn_6Sn_6$ single crystal from 2 to 390 K in **a** 0.1 kOe and **b** 5, 10, 15, and 20 kOe. The transitions T_N, $T_{on,ferri}$, and T_C and T_t are indicated by arrows. **c** *M*–*H* isotherms, in *H* || *ab*-plane at 2, 60, 140, 200, and 360 K. Inset: *M*–*H* curves of 140 and 200 K from 5 to 20 kOe, exhibiting two field-induced steps. **d** The differential susceptibility *dM*/*dH* vs. field at 140 and 200 K. The peaks, marked by 1 and 2, indicate dual metamagnetic fields H^1_{meta} and H^2_{meta} respectively. **e** *M*–*T* data of $ErMn_6Sn_6$ from 2 to 390 K, measured in *H* = 1 kOe and under different constant pressures 0, 0.237, 0.343, 0.606, 0.66, 1.082, and 1.24 GPa. Inset: The data from 340 to 390 K, in which the peak temperature i.e., T_N shifts toward high temperature with the application of pressure. **f** *d*(*MT*)/*dT* vs. *T* plots, confined to the temperature range from 50 to 200 K. The dip temperature is designated as T_C, which increases with the increase of pressure.

from the figure that the magnetization increases with the reduction of temperature from 390 K by exhibiting a peak at 347.03 K. Further reduction of temperature causes down fall of magnetization up to 194 K below which the magnetization increases steeply up to 68 K before undergoing a downturn. The high-temperature peak is designated as antiferromagnetic ordering Néel transition temperature $T_N \sim 347.03$ K from a paramagnetic state. A ferrimagnetic ordering at $T_C \sim 74.02$ K is identified based on the sharp dip in *dM*/*dT* (a first derivative of *M* with respect to *T*). Nevertheless, $T_{mid} \sim 194$ K marks the temperature below which the magnetization increases with the reduction of temperature. This rise of magnetization finds its routes in an enhanced cooperative spin phenomenon and uncompensated magnetic moments of Mn and Er, different from antiferromagnetic ordering. Figure 2b shows *M*–*T* curves under the influence of magnetic fields *H* = 5, 10, 15, and 20 kOe. The lowering of T_N and enhancement of T_C with the increase of magnetic field strength is apparent from Fig. 2b. Considering Fig. 2a, b, the measured temperature range can be classified into four regions *viz.T*-region I ($T \le T_t$), II ($T_t \le T \le T_C$), III ($T_C \le T \le T_N$) and IV ($T \ge T_N$) where T_t is spin-orientation transition. The manifestation of this magnetic phase under the influence of external perturbations such as magnetic field *H* and hydrostatic pressure *p* will be explored in later sections. Figure 2c shows some of the representative isothermal magnetization vs. magnetic field curves measured at ambient pressure and 2, 60, 140, 200, and 360 K. *M*–*H* at 2 and 60 K (below T_C) increases steeply before reaching saturation without any field-induced phase transition. However, *M*–*H* at

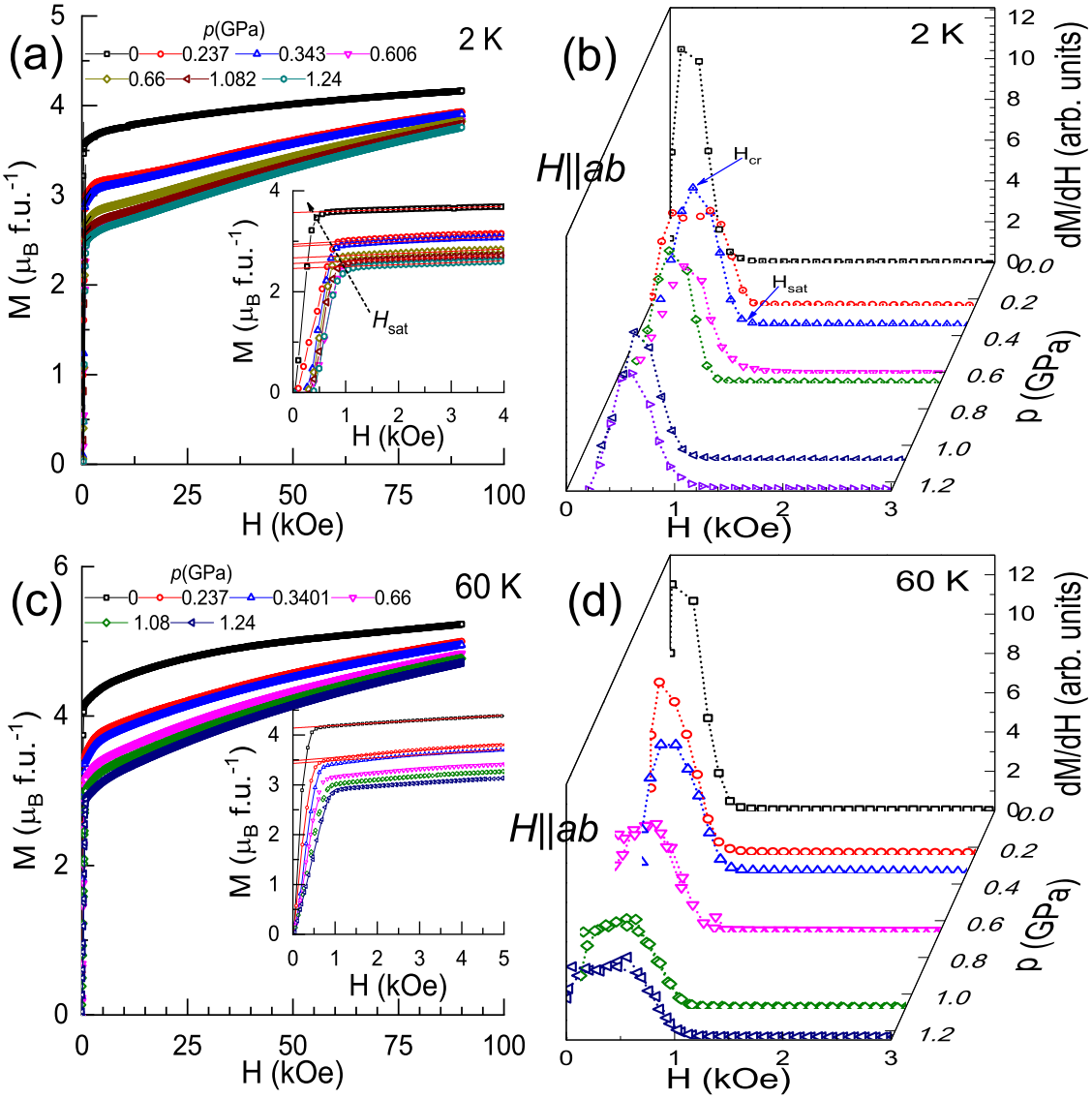

Fig. 3 | Magnetization isotherms and the corresponding differential susceptibilities of $ErMn_6Sn_6$ at 2 K and 60 K in different applied hydrostatic pressures when $H \parallel ab$-plane. An isothermal–isobaric magnetization vs. magnetic field curves (H: 0 → 90 kOe) of $ErMn_6Sn_6$ measured in T region I at **a** 2 K and T region II at **c** 60 K. Insets of **a** and **c** Pressure reduces the spontaneous magnetic moment, the magnetization axis intercept of linearly interpolated M–H down to 0 kOe from 5 kOe. Three-dimensional (3D) plots of the differential susceptibility dM/dH as a function of H and p at **b** 2 K and **d** 60 K. Low-field nonlinear growth of magnetization up to H_{cr} is evident from the linear growth of dM/dH at 2 K while almost linear-growth at 60 K.

140 and 200 K ($T_C < T < T_N$) shows a two-step increment of magnetization before reaching saturation state, as clearly shown in the inset of Fig. 2c. Figure 2d shows the field variation of differential susceptibility (dM/dH) of 140 and 200 K M–H curves. It is evident that 140 and 200 K curves exhibit dual sharp peaks, the field-induced metamagnetic transitions marked as 1 (H^1_{meta}) and 2 (H^2_{meta}). H^1_{meta}, H^2_{meta} for 140 K and 200 K are 9.52, 10.94 kOe, and 14.10, 15.98 kOe, respectively. The effect of pressure on the magnetic properties of $ErMn_6Sn_6$ is explored by making use of isobaric M–T curves in $H = 0.1$ kOe and isothermal–isobaric M–H curves. Figure 2e shows M–T data from 2 to 390 K under the effect of hydrostatic pressures ranging from 0 to 1.24 GPa. The observed dual transitions in 0.1 kOe are found to sustain under pressure. The inset of Fig. 2e shows a high-temperature shift of Néel temperature T_N. Simultaneous enhancement of T_C with pressure is confirmed in Fig. 2f, a plot between $d(MT)/dT$ vs. T.

Further, the effect of pressure on $ErMn_6Sn_6$ is probed by measuring the isothermal magnetization as a function of the magnetic field in T regions I, II, and III under constant applied pressures ranging from 0 to 1.24 GPa. The measurements are carried out by sweeping magnetic field from 0 to 90 kOe in five quadrants (0 → 90 → 0 → −90 → 0 → 90 kOe). Owing to the symmetric nature of the curves, only the first quadrant (0 → 90 kOe) data is shown. $\underline{T}$ region I: Figure 3a shows the first quadrant M–H curves (0 → 90 kOe), measured at 2 K isothermally. Commonly, as shown in the inset of Fig. 3a—limiting the H-axis to 4 kOe, in low-field magnetization grows non-linearly until a certain critical magnetic field, denoted as H_{cr}. H_{cr} is the magnetic field up to which the magnetization grows non-linearly, and H_{sat} is the field at which the saturation begins. These fields are denoted in Fig. 3b—differential susceptibility plots. dM/dH peaks at H_{cr} and becomes field-independent in $H \geq H_{sat}$. Application of magnetic field beyond H_{cr} enforces ferrimagnetic-type (linear M–H) saturation at H_{sat}. The pressure dependence of H_{cr} and H_{sat} are well depicted and determined using Fig. 3b, a three-dimensional plot of differential susceptibility (dM/dH) as a function of H at some representative pressure points. It is noticed that in T region I, attributing to the spin-reorientation, H_{cr} increases while H_{sat} decreases with p, indicating a robust low-field, low-temperature spin-reorientation phase with enhanced magnetic interactions. However, the spontaneous magnetic moment $M_s(\mu_B)$ decreases with pressure. $\underline{T}$ region II: Figure 3c presents

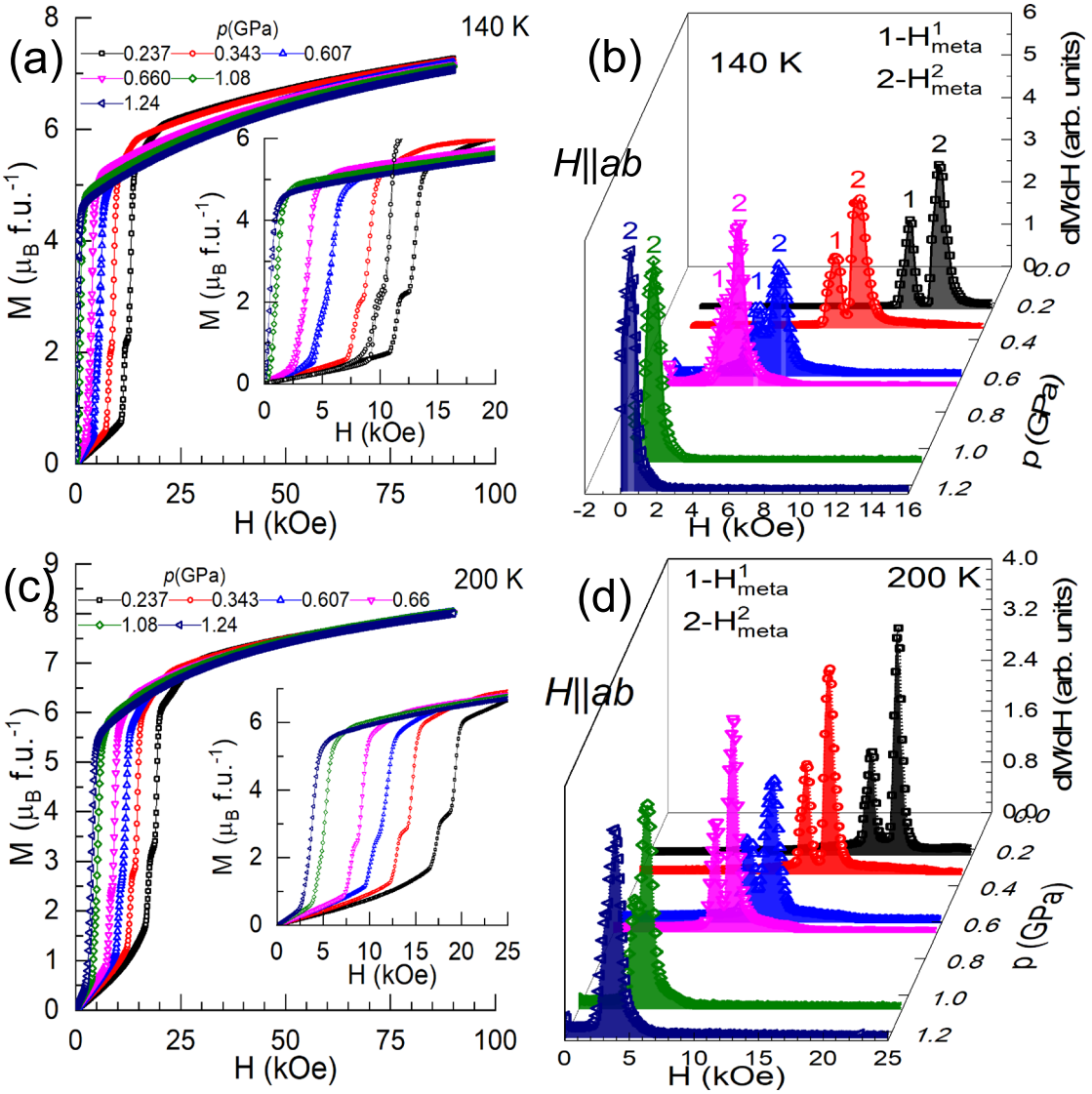

Fig. 4 | Magnetization isotherms and the corresponding differential susceptibilities of $ErMn_6Sn_6$ at 140 K and 200 K in different applied hydrostatic pressures when *H* || *ab*-plane. An isothermal magnetization vs. magnetic field *M*–*H* curves (*H*: 0 → 90 kOe) of $ErMn_6Sn_6$ measured at **a** 140 K and **c** 200 K by applying constant pressures in *T* region III i.e., phase coexistence regime. At *p* = 0.237 GPa, *M* increases quasilinearly with *H* in low fields (dominant antiferromagnetic interactions) up to a certain field above which it undergoes two sudden jumps followed by a linear-like-ferrimagnetic-saturation in fields above H_{sat} ~ 21.19 kOe (at 140 K) and 30.25 kOe (at 200 K). Insets of **a** and **c** *M*–*H* data of 140 K and 200 K, where *H* is limited to 20–25 kOe. An increase in pressure suppresses H_{sat} and unites two sudden jumps. A 3D presentation of the differential susceptibility *dM*/*dH* vs. *H* of **b** 140 K and **d** 200 K under different *p*. At *p* = 0.237 GPa, two distinct sharp peaks at H^1_{meta} = 11.45 and 17.33 kOe and H^2_{meta} = 13.04 and 19.33 kOe, denoted as 1 and 2, represent field-induced metamagnetic transitions at 140 and 200 K, respectively. These two peaks are noticed to convolute into one peak with increasing pressure while shifting the peak position toward lower *H*.

M–*H* isothermal curves measured at 60 K. In low fields, *M*–*H* growth changes from nonlinear to linear in high pressures, as evident from the flat *dM*/*dH* in Fig. 3d. The inset of Fig. 3c shows the field variation of *M* with *H* from 0 to 5 kOe. H_{cr} and H_{sat} increase with *p*. Overall, in *T* regions I and II, magnetization is reversible under field cycling and increases steeply before attaining saturation without any appreciable/noticeable field/pressure-induced manifestations to the ferrimagnetic state. *T* region III: As inferred from *M*–*T* curves of $ErMn_6Sn_6$, it is a coexistence region of antiferromagnetic and ferrimagnetic phases (see Fig. 2d). The effect of pressure on the phase coexistence region is examined by measuring isothermal–isobaric magnetization as a function of magnetic field at 140 and 200 K. Figure 4a, c shows *M*–*H* curves at 140 and 200 K. The system exhibits similar features at 140 and 200 K, however, with enhanced critical and saturation fields at 200 K as compared to that at 140 K. At *p* = 0.237 GPa, *M* grows quasilinearly with *H* up to a certain magnetic field above which it exhibits two sudden jumps before attaining ferrimagnetic saturation-like state. Such sudden jumps are denoted as metamagnetic transitions H^1_{meta} and H^2_{meta}, respectively. In addition, the pressure is seen to suppress the saturation magnetic field and merge metamagnetic transition.

Discussion

Theoretically, the effective magnetic moment of $ErMn_6Sn_6$ is calculated using the formula $\mu^2_{eff,Th.} = n\mu^2_{eff,Er} + m\mu^2_{eff,Mn}$, where *n* and *m* are number of Er and Mn atoms in the unit cell. Experimentally calculated effective magnetic moment $\mu_{eff,Exp.}$ (see Fig. 5a), in *H* = 0.1 kOe, is found be smaller than the calculated theoretical $\mu_{eff,Thr} = 15.38\mu_B$ (*n* = 1, *m* = 6, $\mu_{eff,Er} = 9.59\mu_B$ and $\mu_{eff,Mn} = 4.91\mu_B$). The low effective moment suggests unstable magnetic ground states in 0.1 kOe while hinting at feasible field-induced transitions. However, $\mu_{eff,Exp.}$ in an applied field of 10 kOe is comparable to $\mu_{eff,Thr.}$ value, see Fig. 5a. As per the existing literature, though the magnetic nature of $ErMn_6Sn_6$ in *T* regions I and II is fairly understood[31], the behavior in *T* region III is still intriguing presumably owing to its

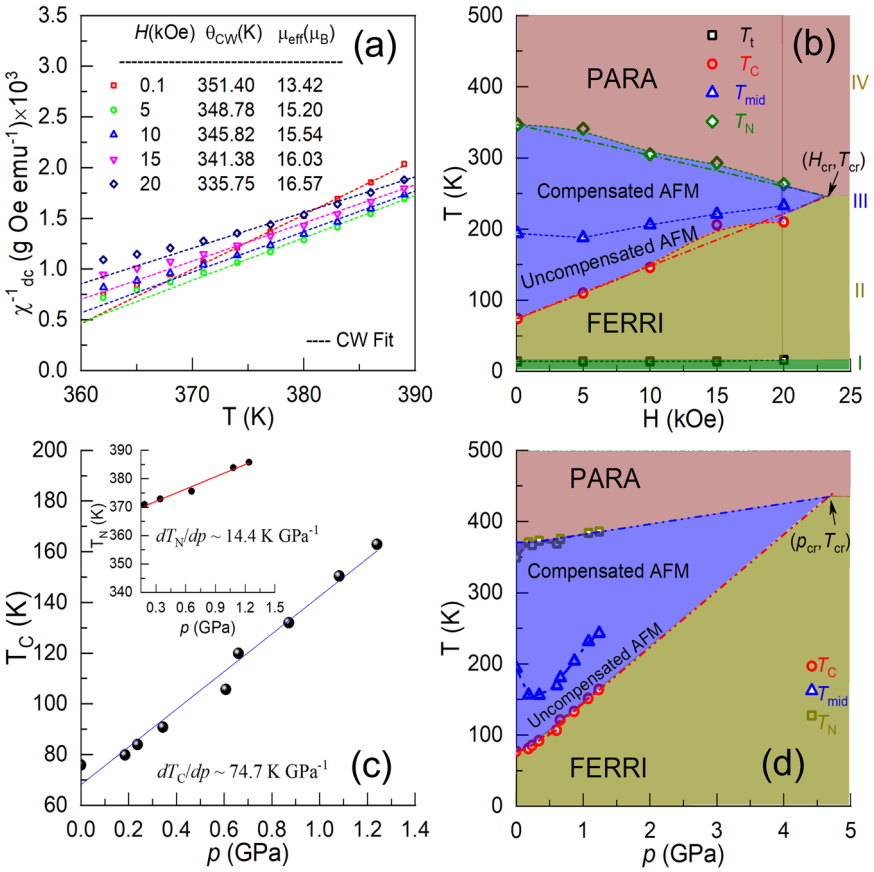

Fig. 5 | Inverse susceptibility, pressure variation of the ferrimagnetic transition temperature, magnetic field- and pressure-driven phase diagrams. **a** An inverse susceptibility $\chi_{dc}^{-1}(T)$ along with Curie–Weiss fits. The resulting fit parameters θ_{CW} and μ_{eff} are shown in the graph. **b** Temperature–field (T–H) phase diagram, distinguishing paramagnetic and ferrimagnetic phases in zero/low-fields, via coexisting ferrimagnetic and antiferromagnetic phases. Magnetic field suppresses the antiferromagnetic phase in about $H = 23.28$ kOe, above which a continuous phase transition from paramagnetic to ferrimagnetic phase. **c** pressure dependence of T_C with a linear fit, showing a slope of about $dT_C/dp = 74.4$ K GPa^{-1}. The slope $dT_C/dp = 79.13$ K GPa^{-1} when the lower bound is limited to 0.237 GPa. **d** Temperature-pressure T–p phase diagram with separating boundaries between ferri, antiferro+ferri, and paramagnetic phases.

complex magnetic structure in zero/low-fields. In such complex situations, a probe using external perturbations facilitates exposure of the underlying magnetic interactions. In this regard, phase diagrams are constructed based on the field and pressure variation of transition temperatures T_N and T_C by referring to M–T curves shown in Fig. 2a, b, e, f. Figure 5a shows the fits of inverse dc-susceptibility ($\chi_{dc}^{-1} \equiv H/M$) from 390 to 360 K, using Curie–Weiss law $\chi(T) = C/(T - \theta_{CW})$ where C is Curie constant and θ_{CW} is paramagnetic Weiss temperature. The fits reveal decreased θ_{CW} from about 351.40 to 335.75 K and enhanced effective magnetic moment of about 13.42 to 16.57μ_B when the field is strengthened from 0.1 to 20 kOe, respectively. H–T phase diagram, illustrating temperature- and field-driven changes to the zero-field magnetic states by revealing four distinct magnetic regimes of $ErMn_6Sn_6$ is drawn in Fig. 5b. In zero- or low-magnetic fields, viewing from the high temperature, T_N separates the paramagnetic (T region IV) and antiferromagnetic phases while T region III, bounded by T_C and T_N, represents the coexistence of ferri and antiferromagnetic phases. The T region II, below T_C, is a ferrimagnetic phase. Furthermore, the field-dependence of $T_{on,fim}$ divides the coexistence phase region into antiferromagnetic dominant ($T_{on,ferri} \le T \le T_N$) and ferrimagnetic dominant ($T_C \le T \le T_{on,fim}$) regimes. In addition, in applied fields of 5 kOe and above, M–T exhibits a dip at T_{upturn}, which is found to be field-independent and serves as the boundary for T region I. Nevertheless, the effect of the magnetic field is reflected in the decrease of T_N and increase of T_C along with a high-temperature shift of $T_{on,ferri}$, inferring the expansion of the ferrimagnetic phase at the cost of the antiferromagnetic phase. Eventually, it is predicted that the field-dependent T_N and T_C meet at a point in H–T space, suggesting a critical point ($H_{cr} = 23.28$ kOe, $T_{cr} = 246.01$ K) in H–T space, indicative of a field-induced continuous phase transition from paramagnetic to ferrimagnetic states above the critical point. Overall, it is understood from the magnetization analysis of $ErMn_6Sn_6$ that the system undergoes consecutive two magnetic transitions at T_N (paramagnetic to antiferromagnetic) and T_C (coexistence phase to ferrimagnetic) with an exception to small spin-reorientation transition at T_t. The application of a magnetic field stabilizes the ferrimagnetic phase by narrowing down the temperature window of the phase coexistence region. The width of the temperature window between T_N and T_C, i.e., $\Delta T_{N\to C}$ is about 273 K in $H = 0.1$ kOe, which reduces by about 220 K at $H = 20$ kOe.

Figure 5c depicts the pressure variation of T_C and (inset) T_N. A linear fit reveals an enhancement rate of about 74.4 and 14.4 K GPa^{-1} respectively. Shown in Fig. 5d is p–T phase diagram based on the pressure-dependence of T_N, $T_{on,fim}$ and T_C. It presents demarcation among ferrimagnetic, magnetic-phase coexistence, and paramagnetic phases. It is evident from the phase diagram that both T_N and T_C simultaneously increase with the increase of pressure. The width of the temperature window between T_N and T_C at $p = 0$ GPa is $\Delta T_{N\to C} = 273$ K, which reduces by about 50.85 K at $p = 1.24$ GPa, despite increasing $T_{N,C}(p)$. At low pressures, there is an indication of enhanced magnetic entropy because of the dominating antiferromagnetic phase, inferred from the shallow $T_{on,ferri}$. Above 0.6 GPa, $T_{on,fim}(p)$ increases, indicating a reduction of the antiferromagnetic phase. The linear fittings of pressure-dependent T_N and T_C above 0.237 GPa resulted in $dT_N/dp \sim 14.4$ K GPa^{-1} and $dT_C/dp \sim 79.13$ K GPa^{-1}. This implies a growing ferrimagnetic phase as compared to that of the antiferromagnetic phase by the application of pressure. Linearly extrapolated dT_N/dp and dT_C/dp meet in p–T space, predicting a critical point ($p_{cr} = 4.736$ GPa, $T_{cr} = 435.78$ K) above which there would be a continuous pressure-induced transition from paramagnetic to ferrimagnetic phase. Overall, it is summarized from the H–T and p–T phase diagrams of $ErMn_6Sn_6$, shown in Figs. 2d and 5d, that H suppresses the antiferromagnetic phase with a critical temperature above $(T_N + T_C)/2$, i.e., lying in the antiferromagnetic-dominated region. On the other hand, p enhances T_N and T_C though, effectively suppresses the antiferromagnetic phase owing to the difference in the rates of increment. However, the critical temperature is found to be beyond the Néel temperature (349.57 K in 0.1 kOe).

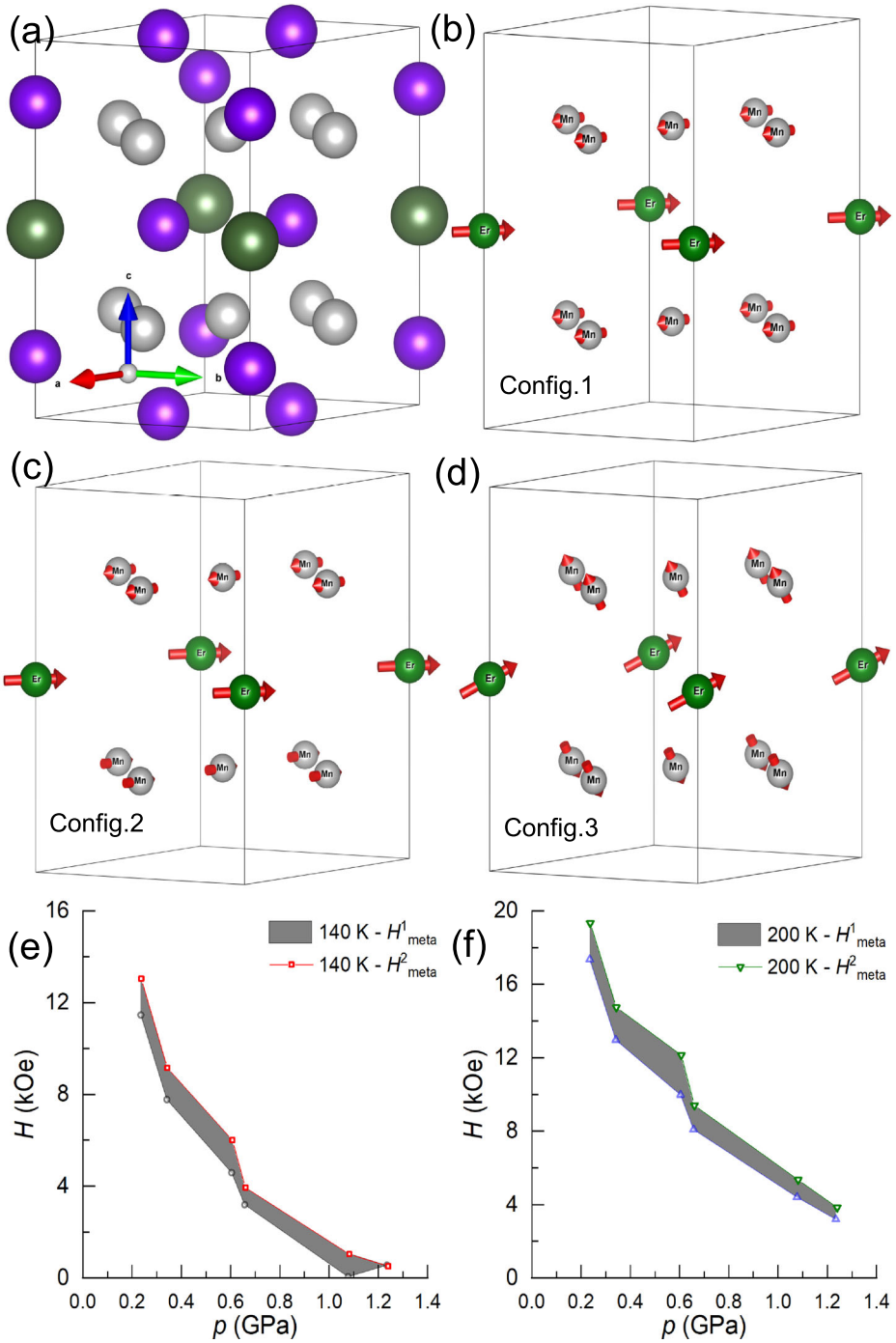

Fig. 6 | Crystal unit cell, schematics of possible projections of magnetic structure and effect of pressure on metamagnetic transition fields at 140 K and 200 K. a Chemical crystalline structure/unit cell of $ErMn_6Sn_6$. Olive, white–gray and blue colors represent Er, Mn, and Sn atoms, respectively. The Er-layer is in between two Mn layers along the *c*-axis. **b**–**d** The representative/proposed magnetic structures of $ErMn_6Sn_6$ along *ab*-plane with different configurations: **b** Config.1—strong AFM—ferromagneticallly arranged Er, Mn^t, and Mn^b moments within the layer and an antiferromagnetic coupling between Er and Mn layers, **c** Config.2—relatively weak AFM—ferromagneticallly arranged Er, Mn^t, and Mn^b moments within the layer and a ferromagnetic coupling between Er and Mn^b and antiferromagnetic coupling between Er and Mn^t layers, **d** Config.3—weak canted AFM—ferromagneticallly arranged Er, Mn^t, and Mn^b moments within the layer and a canted antiferromagnetic coupling between Er–Mn and Mn–Mn inter-layers. **e**, **f** Variation of metamagnetic transition fields with pressure at 140 and 200 K, respectively, indicating the merger of transitions.

Effect of *H* on Region III: It is evident from Fig. 2d that $ErMn_6Sn_6$ exhibits dual metamagnetic transitions in the mixed magnetic phase region. The metamagnetic transition is a magnetic field-induced transition from antiferromagnetic configuration ↑↓↑↓↑↓↑↓ to ferromagnetic configuration (↑↑↑↑↑↑↑↑) or (↓↓↓↓↓↓↓↓) in a field H_{meta}. This is caused by an abrupt flipping of one of the sub-lattices in the direction of external fields. ↑↑↑↑↑↑↑↑ or ↓↓↓↓↓↓↓↓ configurations are according to the sign of the applied magnetic field $+H$ or $-H$, respectively. In the case of a single magnetic transition T_N, the magnitude of H_{meta} depends on the strength of magnetocrystalline anisotropy[33]. However, the degree of complexity increases in materials with dual transitions; high-T_N and low-T_C. Particularly in layered systems, the field-induced effects are governed by the inter-layer magnetic interactions. As shown in Fig. 6a the unit cell of $ErMn_6Sn_6$ in which the magnetic atoms are arranged as follows: Er-atomic layer is sandwiched by top and bottom Mn-atomic layers (Mn^t and Mn^b) along the *c*-axis. Confining to the discussion on the effect of magnetic field in the *ab*-plane, for the present case, three possible inter-layer exchange interactions are *R*-Mn (Er–Mn^b and Er–Mn^t) and Mn–Mn (Mn^b–Mn^t). The representative/proposed magnetic structures of $ErMn_6Sn_6$ along the *ab*-plane are shown in Fig. 6b–d with different configurations (referred to as Config., hereafter). In all of the configurations, the magnetic moments are ferromagnetically arranged within the individual layers. Figure 6b shows Config.1, representing strong antiferromagnetic coupling between Er and Mn layers while Mn–Mn layers interact ferromagnetically. Figure 6c depicts Config.2 in which Er–Mn^b layers interact ferromagnetically, Er–Mn^t and Mn–Mn layers antiferromagnetically, leading to an overall relatively weak

antiferromagnetic exchange interaction in the *ab*-plane. It is important to note that equally energetic configurations can be obtained for Configs.1 and 2 by reversing the spins in each magnetic layer. Figure 6d shows Config.3, in which Er, Mn^t, and Mn^b layers are ferromagnetically aligned in the *ab*-plane with the tilting angle along the *c*-direction. In a canted antiferromagnet, the alternating spins are antiparallel to each other, the spins are canted (tilted) with an angle with respect to each other. In addition, the inter-layer canted angle is different for Mn^b–Er, Er–Mn^t, and Mn^b–Mn^t layers. In this configuration, an extension of the unit cell results in three spirals (triple-spiral) of Mn^b, Er, and Mn^t atoms along the *c*-axis. Such a canted nature between the layers not only weakens the exchange interaction but introduces complex/mixed magnetic phases. Moreover, the reduction of temperature (an otherwise lowering of spin-randomizing factor), reduces the canted angle by favouring ferrimagnetic state over antiferromagnetic configuration.

Here, we discuss the effect of magnetic field anisotropic properties of $ErMn_6Sn_6$. In $H||c$, the externally applied field couples Mn^b, Er, and Mn^t layers, making the magnetic interaction strong, leading to the growth of ferrimagnetic component while simultaneously reducing the antiferromagnetic component. On the other hand, the influence of H on *ab*-plane magnetism is intriguing because of the different configurations of magnetic structure discussed in the previous paragraph, as shown in Fig. 6b–d. In H || *ab*-plane, the applied field acts simultaneously to (i) align the magnetic moments within the individual layers along the *ab*-plane and (ii) strengthen the inter-layer magnetic coupling. Further, the polarization of moments depends on the inter-layer exchange interaction. As per Config.1, it is expected that high fields are required to induce a high magnetic moment state (FM/FIM) because of the strong antiferromagnetic nature. In this configuration, sudden changes in magnetic state can occur at a single H_{meta} since the field acts uniformly on each magnetic layer. As per Config.2 also suggests a single H_{meta}, if any, but at relatively low fields since one of the Mn layers is almost in ferromagnetic alignment with Er magnetic layer. These two configurations do not explain the experimentally obtained dual metamagnetic transitions. In Config.3, the Er-layer acts as a strong key central magnetic layer about which the top and the bottom Mn layers orient. $ErMn_6Sn_6$ has inversion symmetry, meaning Mn^t and Mn^b layers are symmetric about the Er layer. However, considering magnetic structure, the spin orientation directions of Mn^t and Mn^b layers with respect to the Er layer are different (with different tilting angles with temperature), breaking the symmetry despite the similar J strength. Therefore, the layers with weak exchange interaction energy (Mn–Mn) orient at low fields, resulting in H^1_{meta} and the layers with strong exchange interaction energy (Er–Mn) orient at high fields, resulting in H^2_{meta}. This argument is in accordance with the experimentally observed dual metamagnetic transitions as shown in Fig. 2d. At H^1_{meta}, the field overcomes the relatively smaller anisotropic exchange energy and weaker $J(Mn^b—Mn^t)$ (due to larger inter-planer spacing of Mn layers). At H^2_{meta}, the field overcomes the larger anisotropy of Er and stronger exchange interaction energy of Er and Mn layers. This scenario confirms three different tilting angles of Mn^b, Er, and Mn^t magnetic layers in the *ab*-plane and their progression along the *c*-direction, suggesting three spirals in T region III. Similar spiral features were also reported in RMn_6Sn_6 systems in refs. 34–37. Since Er has a large orbital moment causing large magneto-crystalline anisotropy. Hence their Er moments are locked to an easy axis. The exchange interaction energy between Er and Mn layers is strong because of the smaller inter-layer distance as compared to that of Mn–Mn layers.

Effect of H on region III under constant p: It is to be noted from Fig. 4b, d that the external pressure does not only reduce the values of dual metamagnetic transition fields H^1_{meta} (low-intense peak) and H^2_{meta} (high-intense peak) but also simultaneously convolutes low-field peak into the high-field peak, in addition to the reduction of saturation magnetic field. The decrease of H_{meta} (in other words, the spin-flip orientation in low fields) i.e., decreased magnetocrystalline anisotropy, is indicative of enhanced exchange interactions between the magnetic layers. Assuming that the applied pressure in the *ab*-basal plane, the strengthening of magnetic interactions in the inter-layers is ascribed to the following possible reasons; (i) the role of pressure in enhancing the transition temperature (an otherwise strengthening of magnetic interactions) by compressing the lattice is discarded based on an argument that half-Ho doped $ErMn_6Sn_6$ is witnessed to exhibit enhanced T_C from about 74.02 K ($ErMn_6Sn_6$[31]) to about 114 K ($Er_{0.5}Ho_{0.5}Mn_6Sn_6$[38]) with mere no change in the lattice parameter at room temperature, (ii) bending of Mn layers (both above and below the Er-layer) by the application of pressure with sharing corner as the bending point. In such case, the lattice parameter does not shrink, however, the central Mn atoms from top and bottom layers in a unit cell come close to edge sitting Er atoms. This can strengthen the *R*-Mn interaction leading to enhanced magnetic transition temperature with increasing pressure. However, this narration of the effect of pressure does not explain the suppression of one metamagnetic transition in higher pressures, iii) the effect of pressure on the spirals of Er, Mn^t and Mn^b layers is another possibility to discuss. Figure 6e, f shows the variation of H^1_{meta} and H^2_{meta} with pressure at $T = 140$ K and 200 K, respectively. The phase diagrams illustrate the pressure-induced tricritical point (emergence of a second-order continuous transition) by ending the first-order phase transition (metamagnetism)[39–41]. The external perturbations (magnetic field and pressure) induced changes in the magnetic ground state of $ErMn_6Sn_6$ are explored. The double metamagnetic transitions in the compensated and uncompensated antiferromagnetic regimes (bounded by T_C and T_N) find routes in the triple (Er, Mn^b, and Mn^t) spiral magnetic layers propagating in the *c*-direction. Both magnetic field and pressure tune the system towards a critical point conventionally and unconventionally, respectively. In addition, above the critical point, the system continuously transits from the paramagnetic to the ferrimagnetic phase in the presence of constant perturbation. Moreover, the system drives towards a tricritical point by manifesting the triple spirals through the simultaneous application of pressure and magnetic field.

Conclusions

The magnetic field and/or hydrostatic pressure manifested magnetic properties of a kagome layered single crystal $ErMn_6Sn_6$ are investigated and demonstrated through temperature-magnetic field/pressure phase diagrams. Mainly, it exhibits dual magnetic transitions namely antiferromagnetic with $T_N \sim 347$ K and ferrimagnetic with $T_C \sim 74$ K. The magnetic field is noticed to suppress T_N and enhance T_C along with dual metamagnetic transitions in the T-regime of mixed-magnetic phases. The reason for dual metamagnetic transitions is attributed to the spiral behavior of magnetic (Er, Mn^t, and Mn^b) layers in a unit cell. Essentially, in the presence of high magnetic fields, metamagnetic transitions are suppressed, leading to the field-induced critical point of ($T_{cr} = 246.01$ K, $H_{cr} = 23.28$ kOe) above which a continuous phase transition from paramagnetic to ferrimagnetic phase occurs. On the other hand, an iso-field ($H = 1$ kOe) magnetization data under the influence constant p reveal increasing T_C and T_N at a giant growth rate of about 74.4 K GPa^{-1} and 14.4 K GPa^{-1} respectively. In addition, isothermal magnetization measurements unveil the unification/merger of dual metamagnetic peaks into one by possibly suppressing the triple spirals to strengthen the interactions among magnetic layers. Despite increasing T_C and T_N, a continuous phase transition from paramagnetic to ferrimagnetic state is predicted to occur at a pressure-induced critical point ($T_{cr} = 435.78$ K, $p_{cr} = 4.736$ GPa) owning to the difference in the growth rates of T_C and T_N. This is far above the zero-field antiferromagnetic transition temperature, distinct from that of the magnetic field-induced critical point. The above results indicate a unique way of tuning the magnetic properties of kagome layered magnets by applying magnetic field and pressure simultaneously. Further to explore, neutron diffraction patterns in the presence of magnetic field and pressure are desired to understand the manifestation of chiral/spiral Er and Mn layers.

Methods

Synthesis

The single crystals of $ErMn_6Sn_6$ were prepared by flux growth technique using Sn as a flux[31,38]. In this method, high pure elements of at least 99.95%

Er, Mn, and Sn were weighed in the ratio of 1:6:25 and loaded into Canfield Crucibles and a hole strainer was used in between the crucibles. The crucible set was evacuated several times, flushed with Argon gas, and sealed in an evacuated quartz tube. The sample tubes were sintered in a high-temperature furnace at 1100 °C for 10 h and then cooled down to 600 °C with a slow cooling rate of 1.6 °C per hour. Single crystals were obtained by centrifuging the crucibles. The phase purity of the crystals was checked by collecting the X-ray diffraction patterns using the Rigaku Miniflex 600 at room temperature using copper K_α radiation. Temperature-dependent X-ray diffraction was carried out on powder samples using an Anton Paar XRDynamic 500 powder diffractometer.

Magnetization

The magnetic measurements were performed on a flat crystal of $ErMn_6Sn_6$ with size of about 2 mm^2 by using a Physical Property Measurement System (PPMS Dynacool, Quantum Design, Inc. USA), equipped with a vibrating sample magnetometer (VSM). The data were collected in the temperature range between 2 and 400 K, under applied field up to 90 kOe and under hydrostatic pressure up to 1.24 GPa both as a function of temperature, $M(T)$, and applied magnetic field, $M(H)$, by orienting the applied field, H, parallel to ab-plane ($H \parallel ab$). The pressure-dependent magnetization was measured using a BeCu HPC-33 piston-type pressure cell, where the sample was immersed in a pressure-transmitting medium (Daphne oil) in a Teflon cell.

Data availability

The data that support the findings of this study are available from the corresponding author upon reasonable request.

Received: 5 February 2024; Accepted: 21 June 2024;
Published online: 01 July 2024

References

1. Bernevig, B. A., Hughes, T. L. & Zhang, S.-C. Quantum spin hall effect and topological phase transition in hgte quantum wells. *Science* **314**, 1757–1761 (2006).
2. Moore, J. E. & Balents, L. Topological invariants of time-reversal-invariant band structures. *Phys. Rev. B* **75**, 121306 (2007).
3. Fu, L. & Kane, C. L. Topological insulators with inversion symmetry. *Phys. Rev. B* **76**, 045302 (2007).
4. König, M. et al. Quantum spin hall insulator state in hgte quantum wells. *Science* **318**, 766–770 (2007).
5. Hsieh, D. et al. A topological Dirac insulator in a quantum spin hall phase. *Nature* **452**, 970–974 (2008).
6. Moore, J. The birth of topological insulators. *Nature* **464**, 194–198 (2010).
7. Cava, R. J., Ji, H., Fuccillo, M. K., Gibson, Q. D. & Hor, Y. S. Crystal structure and chemistry of topological insulators. *J. Mater. Chem. C* **1**, 3176–3189 (2013).
8. Kumar, N., Guin, S. N., Manna, K., Shekhar, C. & Felser, C. Topological quantum materials from the viewpoint of chemistry. *Chem. Rev*. **121**, 2780–2815 (2021).
9. Yu, R. et al. Quantized anomalous hall effect in magnetic topological insulators. *Science* **329**, 61–64 (2010).
10. Jia, S., Xu, S.-Y. & Hasan, M. Z. Weyl semimetals, fermi arcs and chiral anomalies. *Nat. Mater.* **15**, 1140–1144 (2016).
11. Han, T. et al. Fractionalized excitations in the spin-liquid state of a kagome-lattice antiferromagnet. *Nature* **492**, 406–410 (2012).
12. Yin, J.-X. et al. Negative flat band magnetism in a spin-orbit-coupled correlated kagome magnet. *Nat. Phys.* **15**, 443–448 (2019).
13. Tang, E., Mei, J.-W. & Wen, X.-G. High-temperature fractional quantum hall states. *Phys. Rev. Lett.* **106**, 236802 (2011).
14. Xu, G., Lian, B. & Zhang, S.-C. Intrinsic quantum anomalous hall effect in the kagome lattice $cs_2limn_3f_{12}$. *Phys. Rev. Lett.* **115**, 186802 (2015).
15. Mazin, I. I. et al. Theoretical prediction of a strongly correlated Dirac metal. *Nat. Commun.* **5**, 4261 (2014).
16. Zhang, H., Feng, H., Xu, X., Hao, W. & Du, Y. Recent progress on 2d kagome magnets: Binary tmsnn (t = fe, co, mn). *Adv. Quantum Technol.* **4**, 2100073 (2021).
17. Morali, N. et al. Fermi-arc diversity on surface terminations of the magnetic weyl semimetal $co_3sn_2s_2$. *Science* **365**, 1286–1291 (2019).
18. Yin, J.-X. et al. Quantum-limit chern topological magnetism in $tbmn_6sn_6$. *Nature* **583**, 533–536 (2020).
19. Wang, Q. et al. Field-induced topological hall effect and double-fan spin structure with a *c*-axis component in the metallic kagome antiferromagnetic compound $\mathrm{Ymn_6sn_6}$. *Phys. Rev. B* **103**, 014416 (2021).
20. Asaba, T. et al. Anomalous hall effect in the kagome ferrimagnet $\mathrm{gdmn_6sn_6}$. *Phys. Rev. B* **101**, 174415 (2020).
21. Ma, W. et al. Rare earth engineering in $\mathrm{rmn_6sn_6}$ (r = Gd − Tm, lu) topological kagome magnets. *Phys. Rev. Lett.* **126**, 246602 (2021).
22. Malaman, B., Venturini, G. & Roques, B. New ternary stannides: Mmn_6sn_6 (m = sc, y, sm, gd-tm, lu) and $scfe_6sn_6$. *Mater. Res. Bull.* **23**, 1629–1633 (1988).
23. Teatum, E., Gschneidner Jr, K. A. & Waber, J. Rep LA-4003 (NTIS, Springfield, VA, 1968).
24. Venturini, G., Idrissi, B. E. & Malaman, B. Magnetic properties of rmn_6sn_6 (r = sc, y, gd-tm, lu) compounds with $hffe_6ge_6$ type structure. *J. Magn. Magn. Mater.* **94**, 35–42 (1991).
25. Malaman, B. et al. Magnetic properties of rmn_6sn_6 (r = gd-er) compounds from neutron diffraction and mössbauer measurements. *J. Magn. Magn. Mater.* **202**, 519–534 (1999).
26. Idrissi, B. C. E., Venturini, G., Malaman, B. & Fruchart, D. Magnetic structures of $tbmn_6sn_6$ and $homn_6sn_6$ compounds from neutron diffraction study. *J. Less Common Met.* **175**, 143–154 (1991).
27. Venturini, G., Fruchart, D. & Malaman, B. Incommensurate magnetic structures of rmn_6sn_6(r = sc, y, lu) compounds from neutron diffraction study. *J. Alloy. Compd.* **236**, 102–110 (1996).
28. Clatterbuck, D. M. & Gschneidner Jr, K. A. Magnetic properties of rmn_6sn_6 (r = tb, ho, er, tm, lu) single crystals. *J. Magn. Magn. Mater.* **207**, 78–94 (1999).
29. Gao, L. et al. Anomalous hall effect in ferrimagnetic metal rmn6sn6 (r = tb, dy, ho) with clean mn kagome lattice. *Appl. Phys. Lett.* **119**, 092405 (2021).
30. Wang, B. et al. Magnetotransport properties of the kagome magnet $\mathrm{tmmn_6sn_6}$. *Phys. Rev. B* **106**, 125107 (2022).
31. Dhakal, G. et al. Anisotropically large anomalous and topological hall effect in a kagome magnet. *Phys. Rev. B* **104**, L161115 (2021).
32. Yazdi, S. T., Tajabor, N., Roknabadi, M. R., Behdani, M. & Pourarian, F. Magnetoelastic properties of $ermn_6sn_6$ intermetallic compound. *J. Magn. Magn. Mater.* **324**, 723–728 (2012).
33. Ashcroft, N. & Mermin, N. *Solid State Physics* (Saunders College Publishing, Fort Worth, 1976).
34. Rozenfeld, E. V., Mushnikov, N. V. & Dyakin, V. V. Nested spirals in layered magnets. *Phys. Met. Metallogr.* **107**, 557–568 (2009).
35. Fruhling, K., Yao, X., Streeter, A. & Tafti, F. Characterization of the magnetocaloric effect in rmn6sn6 including high-entropy forms. *Mater. Chem. Phys.* **319**, 129230 (2024).
36. Ghimire, N. J. et al. Competing magnetic phases and fluctuation-driven scalar spin chirality in the kagome metal ymn₆sn₆. *Sci. Adv.* **6**, eabe2680 (2020).
37. Bhandari, H. et al. Magnetism and fermiology of kagome magnet ymn6sn4ge2. *npj Quantum Mater.* **9**, 6 (2024).
38. Casey, J. et al. Spin-flop quasi metamagnetic, anisotropic magnetic, and electrical transport behavior of ho substituted kagome magnet $\mathrm{ermn_6sn_6}$. *Phys. Rev. Mater.* **7**, 074402 (2023).
39. Samatham, S. S., Barua, S. & Suresh, K. G. Spin-flop quasi-first order phase transition and putative tricritical point in gd_3co. *J. Magn. Magn. Mater.* **444**, 439 (2017).

40. Samatham, S. S. & Ganesan, V. Critical behavior, universal magnetocaloric, and magnetoresistance scaling of mnsi. *Phys. Rev. B* **95**, 115118 (2017).
41. Strydom, A. M. Antiferromagnetic ordering and metamagnetism in prcusi. *Eur. Phys. J. B* **74**, 9–18 (2010).

Acknowledgements

This work was performed at the State University of New York (SUNY), Buffalo State University, and was supported by the National Science Foundation, Launching Early-Career Academic Pathways in the Mathematical and Physical Sciences (LEAPS-MPS) program under Award No. DMR-2213412. J.C. acknowledges financial support from the Office of Undergraduate Research, SUNY, Buffalo State University. S.S.S. acknowledges the Science and Engineering Research Board (SERB), Govt. of India, for the financial support through the Core Research Grant (Grant No. CRG/2022/007993). T.S. acknowledges support from NSF DMR-2219906. A.M.S. and T.S. performed the work at the National High Magnetic Field Laboratory, which is funded by the National Science Foundation, award DMR-2128556, and the State of Florida.

Author contributions

J.C. contributed to the design of experiments and characterization and contributed to data analysis. S.S.S. performed data interpretation and drafted the original paper. VY provided scientific comments and data interpretation. C.B. contributed to magnetization measurements at ambient pressure. A.P. conceived the idea, acquired the funding, supervised and guided the study, and data interpretation. All authors provided comments and edits during the preparation of the paper. T.S. and A.M.S. conducted temperature-dependent X-ray diffraction and SEM-EDS measurements, and data analysis.

Competing interests

The authors declare no competing interests.

Additional information

Supplementary information The online version contains supplementary material available at https://doi.org/10.1038/s43246-024-00552-x.

Correspondence and requests for materials should be addressed to Arjun K. Pathak.

Peer review information *Communications Materials* thanks the anonymous reviewers for their contribution to the peer review of this work. Primary Handling Editor: Aldo Isidori.